

# The DTU geomagnetic field parent model and derived IGRF-14 candidate models

Clemens Kloss, Christopher C. Finlay, Nils Olsen, Lars Tøffner-Clausen,  
Nicolas Gillet, Alexander Grayver

1 October 2024

## 1 Introduction

This technical note provides information on the parent field model prepared by the Technical University of Denmark (DTU) in order to extract IGRF-14 candidate models: IGRF-2025, DGRF-2020, and the predictive average SV-2025-2030.

This parent model is an extension of the CHAOS model series (Finlay et al., 2020; Finlay et al., 2016, 2015; Olsen et al., 2009, 2010, 2006, 2014) with notable differences compared to the previous generation CHAOS-7. Concerning the input data, in addition to using the latest *Swarm* satellite and ground-based geomagnetic observatory data, the model includes scalar data from the China Seismo-Electromagnetic Satellite (CSES) mission and vector data from the Macau Science Satellites 1 mission (MSS-1). Moreover, the amount of platform magnetometer data from the CryoSat2 satellite has been increased to cover not only the gap period between the end of the CHAMP mission in August 2010 and the launch of *Swarm* in November 2014 but also the period thereafter until July 2024. On the modeling side, the parent model includes a representation of the ionospheric field due to electric currents in the ionospheric E-layer based on the parameterization of the AMPS model (Laundal et al., 2018). Co-estimation of the ionospheric field, including in polar region where it is significant even on the night side, leads to small differences in the internal field particularly in the near zonal terms. The temporal regularization of the internal field has been improved compared with CHAOS-7. Here, it is based on temporal covariances extracted from geodynamo simulations (Aubert, 2023; Gillet et al., 2024), rather than on minimizing the square of the radial field acceleration integrated over the core surface, which tends to artificially suppress field variations at high degree.

## 2 Magnetic datasets

The DTU parent model for the IGRF-14 is based on satellite data from Ørsted, CHAMP, SAC-C, CryoSat2, *Swarm*, CSES and MSS-1, as well as secular variation data from geomagnetic observatories.

### 2.1 Satellite magnetic data

From the Ørsted satellite, we used scalar magnetic field (intensity) data between March 1999 and June 2013, and vector data between March 1999 and December 2005, at 1 min sampling. In addition, we included along-track scalar difference data obtained from 15 s samples of the scalar data.

From the CHAMP satellite, we included vector data between August 2000 and September 2010, sub-sampled to 1 min, and only when both star cameras were active to provide attitude information. Similar to Ørsted, we included along-track scalar difference data obtained from 15 s scalar data samples. In addition, we made use of along-track vector difference data by differencing the 15 s samples of vector data.

The SAC-C satellite provided scalar data between January 2001 and December 2004 at 1 min sampling.

From CryoSat2, we used vector data collected by the platform magnetometer FGM1, version 0304, between April 2010 and July 2024, sub-sampled to 1 min samples. These data have been corrected and calibrated (Olsen et al., 2020). To reduce the intrinsic noise in the data, we averaged the initial 4 s data over 20 s intervals in the magnetometer frame, before sub-sampling the data to obtain 1 min samples. This averaging was performed through a robust linear fit using Huber weights after removing from the data the field model predictions provided in the data product files. The necessary rotations of the model predictions into the magnetometer frame were carried out with the attitude information available in the data product files and the alignment parameters of the initial calibration of the version 0304 data files.

From the *Swarm* satellite mission, we included vector data, versions 0602/0605/0606, for the three satellites, Swarm-A (Swarm Alpha), Swarm-B (Swarm Bravo), and Swarm-C (Swarm Charlie), between 26 November 2013

and 4 August 2024, each with an initial sampling of 15 s. To have a similar amount of data from the satellite trio compared to the CHAMP period, we sub-sampled the *Swarm* data by a factor of 4, providing data from each satellite at 1 min sampling. However, we further sub-sampled the data from Swarm-A and Swarm-C, which are always flying next to each other, by a factor of 2, resulting in 2 min data for this satellite pair. Along-track scalar and vector difference data were obtained from the 15 s sub-sampled data for each satellite separately. In addition, by differencing the scalar and vector data from the side-by-side flying Swarm-A and Swarm-C satellites, we obtained east-west scalar and vector difference data. Similar to the vector data, we sub-sampled the scalar and vector difference data to have 1 min for Swarm-B and 2 min data for each of Swarm-A and Swarm-C.

From the CSES mission, we made use of the scalar data from the CSES-01 satellite between July 2018 and December 2023, which we sub-sampled from the initial 1 s to 1 min data. Note that we did not use the vector data from CSES-01.

Finally, from the MSS-1 mission, we used vector data provided by the MSS-1A satellite between 2 November 2023 and 31 July 2024, which we sub-sampled to 1 min data. Here, we only used the vector data and not the scalar data available in the product files.

To minimize the effect of field-aligned currents in the polar regions during the modeling, we converted vector data at QD latitudes  $|\lambda_{\text{QD}}| > 55^\circ$  to scalar data. Concerning the vector difference data, we only used this type of data at non-polar latitudes and simply removed it in the polar regions.

## 2.2 Ground observatory magnetic data

To provide additional constraints on the secular variation, we used annual differences of revised monthly means of vector data provided by geomagnetic observatories between July 1997 and July 2024.

The revised monthly means were computed by averaging quality-checked hourly means from the BGS AUX\_OBS data product version 0141 (Macmillan et al., 2013) from 185 geomagnetic observatories that provided data between 1999 and 2024, after removing ionospheric field predictions (inducing plus induced) from the CI field model (Sabaka et al., 2018), version 1010, and predictions of the large-scale magnetospheric field (inducing plus induced) from a preliminary CHAOS-type field model and *RC* index (Olsen et al., 2014). The averaging was performed by a robust method based on Huber weights (Huber, 2004) using data from all local times and latitudes.

IAGA site codes for the geomagnetic observatories used for the DTU parent model spanning 1999 to 2024 are: AAA, AAE, ABG, ABK, AIA, ALE, AMS, AMT, API, AQU, ARS, ASC, ASP, BDV, BEL, BFE, BFO, BGY, BJV, BLC, BMT, BNG, BOU, BOX, BRD, BRW, BSL, CBB, CBI, CDP, CKI, CLF, CMO, CNB, CNH, COI, CPL, CSY, CTA, CTS, CYG, CZT, DED, DLR, DLT, DOB, DOU, DRV, DUR, EBR, ELT, ESA, ESK, EYR, FCC, FRD, FRN, FUQ, FUR, GAN, GCK, GDH, GLM, GNA, GNG, GUA, GUI, GZH, HAD, HBK, HER, HLP, HON, HRB, HRN, HTY, HUA, HYB, IPM, IQA, IRT, IZN, JAI, JCO, KAK, KDU, KEP, KHB, KIR, KIV, KMH, KNY, KNZ, KOU, KSH, LER, LIV, LMM, LNP, LON, LOV, LRM, LRV, LVV, LYC, LZH, MAB, MAW, MBO, MCQ, MEA, MGD, MIZ, MMB, MNK, MOS, MZL, NAQ, NCK, NEW, NGK, NGP, NMP, NUR, NVS, ORC, OTT, PAF, PAG, PBQ, PEG, PET, PHU, PIL, PND, PPT, PST, QGZ, QIX, QSB, QZH, RES, SBA, SBL, SFS, SHE, SHL, SHU, SIL, SIT, SJG, SOD, SPG, SPT, SSH, STJ, STT, SUA, TAM, TAN, TDC, TEO, TFS, THJ, THL, THY, TIR, TRO, TRW, TSU, TUC, UJJ, UPS, VAL, VIC, VNA, VOS, VSK, VSS, WHN, WIC, WIK, WNG, YAK, YKC. Fig. 1 shows a map with the locations of these geomagnetic observatories.

## 2.3 Data selection

We selected satellite scalar, vector and vector difference data according to the following criteria for geomagnetic quiet conditions:

- $Hp30 \leq 2^\circ$  for data at non-polar latitudes,  $|\lambda_{\text{QD}}| \leq 55^\circ$
- $\left| \frac{dRC}{dt} \right| \leq 2 \text{nT h}^{-1}$
- $\epsilon \leq 2.4$ , averaged over the previous 2 h
- strictly positive Interplanetary Magnetic field (IMF)  $B_z$ , averaged over the previous 2 h
- IMF  $B_y \leq 3 \text{nT}$ , averaged over the previous 2 h, for satellite data observed in the northern hemisphere and IMF  $B_y \geq -3 \text{nT}$  for data in the southern hemisphere

The  $Hp30$  index (Matzka et al., 2024; Yamazaki et al., 2022) is a 30 min index expressing the level of geomagnetic disturbance as observed by mid-latitude geomagnetic observatories. It is similar to the 3-hourly  $K_p$  index (Matzka et al., 2021a; Matzka et al., 2021b) but has a higher time resolution and not an upper limit

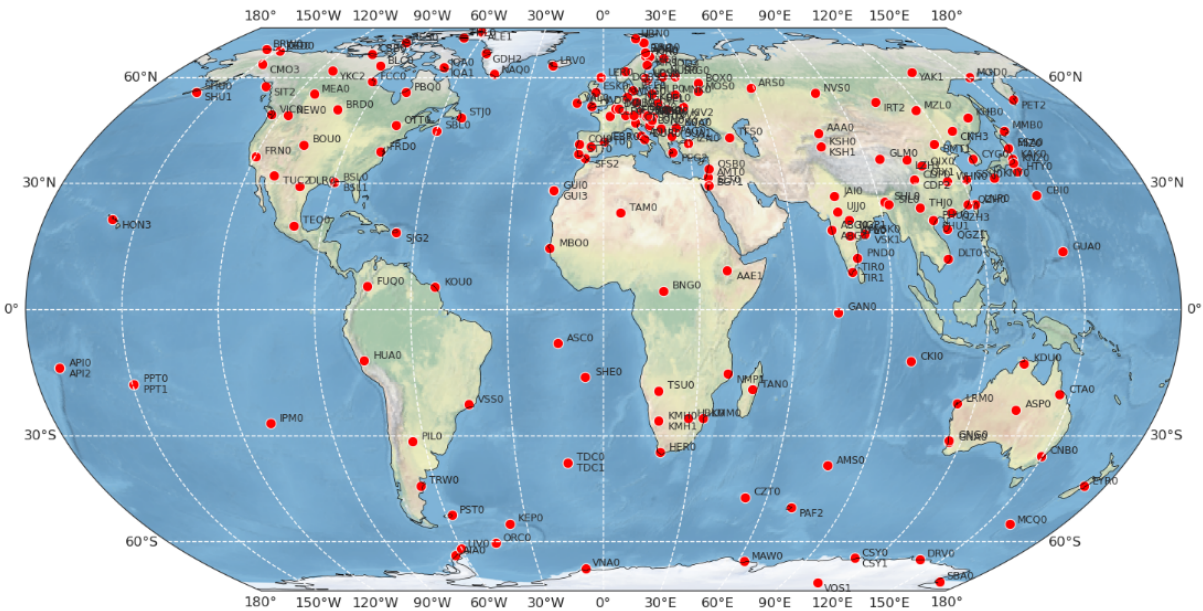


Figure 1: Map showing the locations of the geomagnetic observatories used for the construction of the DTU parent model for IGRF-14.

in magnitude. Newell's coupling function  $\epsilon$  (Newell et al., 2007) is a measure of the rate of magnetic field reconnection on the dayside magnetopause and is defined as

$$\epsilon = 10^{-3} v^{4/3} B_t^{2/3} \sin(|\theta_c|/2)^{8/3} \quad (1)$$

where  $v$  is the solar wind speed in  $\text{km s}^{-1}$  along the Geocentric Solar Magnetospheric (GSM) x-axis,  $B_t = \sqrt{B_{\text{IMF},y}^2 + B_{\text{IMF},z}^2}$  in nT is the tangential field intensity of the IMF in the GSM frame, and the IMF clock angle is  $\theta_c = \arctan 2(B_{\text{IMF},z}, B_{\text{IMF},y})$ . The  $RC$  index, similar to the  $Dst$ -index (Sugiura et al., 1991), is an hourly index describing the strength of the magnetospheric ring current, designed to have a stable baseline (Olsen et al., 2014). Here in a modification of the procedure described in Olsen et al., 2014 the  $RC$  index was derived using data from 14 mid and low latitude observatories covering different longitude sectors (ASP, BOU, CLF, FRD, GUA, HER, HON, KAK, KOU, LRM, ASC, NGK, SJG and SPT) considering data from all local times and carrying out a correction for the ionospheric and induced field using the CI model (Sabaka et al., 2018), version 1001.

Concerning the scalar difference data, we used the same selection criteria but slightly relaxed those based on the  $Hp30$  and  $RC$  indices:

- $Hp30 \leq 3^\circ$  for non-polar data
- $|\frac{dRC}{dt}| \leq 3 \text{nT h}^{-1}$

We flagged but did not remove sunlit data for zenith angles  $\zeta < 100^\circ$  in order to have data on the dayside available for the estimation of the ionospheric field model. Flagged data with zenith angles  $\zeta < 100^\circ$  were not used to constrain the internal and magnetospheric parts of the model (see details in Sect. 3.2).

In total, we estimated the geomagnetic field from 3 127 895 scalar data, 2 839 805 vector data, 37 963 SV vector data from magnetic observatories, 3 831 375 scalar difference data, and 1 517 253 vector difference data. Tab. 1 summarizes the types and amounts of magnetic data provided by the satellites and the geomagnetic observatories.

Fig. 2 shows stacked histograms of the amount of selected satellite and ground observatory data in 3-month bins.

## 3 Field modeling

### 3.1 Model parameterization

We represent the magnetic field as  $\mathbf{B} = -\nabla V$ , the negative gradient a scalar magnetic potential  $V = V^{\text{int}} + V^{\text{ext}}$ , where  $V^{\text{int}}$  and  $V^{\text{ext}}$  represent the potential due to internal and external sources of the field, respectively. We

Table 1: Summary of the ground observatory and satellite data used during the field modeling. Swarm-AC refers to difference data between Swarm-A and Swarm-C.

Data source	Scalar	Vector	Scalar difference	Vector difference	SV vector
Ørsted	849 487	96 190	473 803	n.a.	n.a.
CHAMP	258 599	318 875	521 997	155 345	n.a.
SAC-C	158 656	n.a.	n.a.	n.a.	n.a.
CryoSat2-1	634 367	942 111	n.a.	n.a.	n.a.
Swarm-A	231 917	353 759	365 075	174 624	n.a.
Swarm-B	462 166	707 851	729 689	349 532	n.a.
Swarm-C	232 533	355 055	366 322	175 334	n.a.
Swarm-AC	n.a.	n.a.	1 374 489	662 418	n.a.
CSES	300 170	n.a.	n.a.	n.a.	n.a.
MSS-1	n.a.	65954	n.a.	n.a.	n.a.
Observatories	n.a.	n.a.	n.a.	n.a.	37 963

expand these potentials into spherical harmonics (SH) using geographic and magnetic coordinate systems, depending on the source considered. To distinguish between external sources in the magnetosphere and ionosphere, we write  $V^{\text{ext}} = V^{\text{mag}} + V^{\text{ion}}$ , where  $V^{\text{mag}}$  represents the magnetospheric field and  $V^{\text{ion}}$  the ionospheric field.

Tab. 2 summarizes the most important setup parameters of our parent model. Full details of the model parameterization are given in the following sections.

Table 2: Summary of setup parameters defining the model.

Setup parameter	Description	Value
$N_{\text{int}}$	Maximum SH degree of the internal field	70
$N_{\text{tdep}}$	Maximum SH degree of the time-dependent internal field	20
$k$	B-spline order of the time-dependent internal field	6
$\Delta t_k$	B-spline knot spacing (incl. 6-fold endpoint multiplicity)	0.5 yr
$t_s$	Start time of the internal field model in decimal years	1997.1
$t_e$	End time of the internal field model in decimal years	2025.1
$N_{\text{SM}}^{\text{mag}}$	Maximum SH degree of the inner magnetospheric field	2
$N_{\text{GSM}}^{\text{mag}}$	Maximum SH degree of the outer magnetospheric field (only $m = 0$ terms)	2
$\Delta t_{\text{SM}}$	Bin size for degree-1 $RC$ baseline corrections	30 days
$N^{\text{ion}}$	Maximum SH degree of the ionospheric field	45
$M^{\text{ion}}$	Maximum SH order of the ionospheric field	3

### 3.1.1 Internal field

We represent the potential due to internal sources by the expansion

$$V^{\text{int}}(t, r, \theta, \phi) = a \sum_{n=1}^{N^{\text{int}}} \sum_{m=-n}^n \left(\frac{a}{r}\right)^{n+1} g_n^m(t) Y_n^m(\theta, \phi), \quad (2)$$

where  $a = 6371.2$  km is the mean spherical reference radius of the Earth,  $N^{\text{int}} = 70$  is the maximum truncation degree for the internal field,  $t$  is time,  $r$  is the radius,  $\theta$  is the spherical co-latitude, the angular distance from the geographic north pole, and  $\phi$  is the longitude,  $g_n^m$  are the spherical harmonic (SH) coefficients for degree  $n$  and order  $m$ , and  $Y_n^m$  are the corresponding SH functions defined as

$$Y_n^m(\theta, \phi) = \begin{cases} \cos(m\phi) \mathcal{P}_n^m(\cos \theta), & m \geq 0 \\ \sin(|m|\phi) \mathcal{P}_n^{|m|}(\cos \theta), & m < 0 \end{cases} \quad (3)$$

where  $\mathcal{P}_n^m$  are the associated Legendre functions.

To represent the slowly time-varying internal field on large length-scales, we further expand the Gauss coefficients for  $n \leq N_{\text{tdep}} = 20$  in terms of order- $k$  B-splines

$$g_n^m(t) = \sum_{j=1}^J g_{n,j}^m \mathcal{B}_{k,j}(t), \quad (4)$$

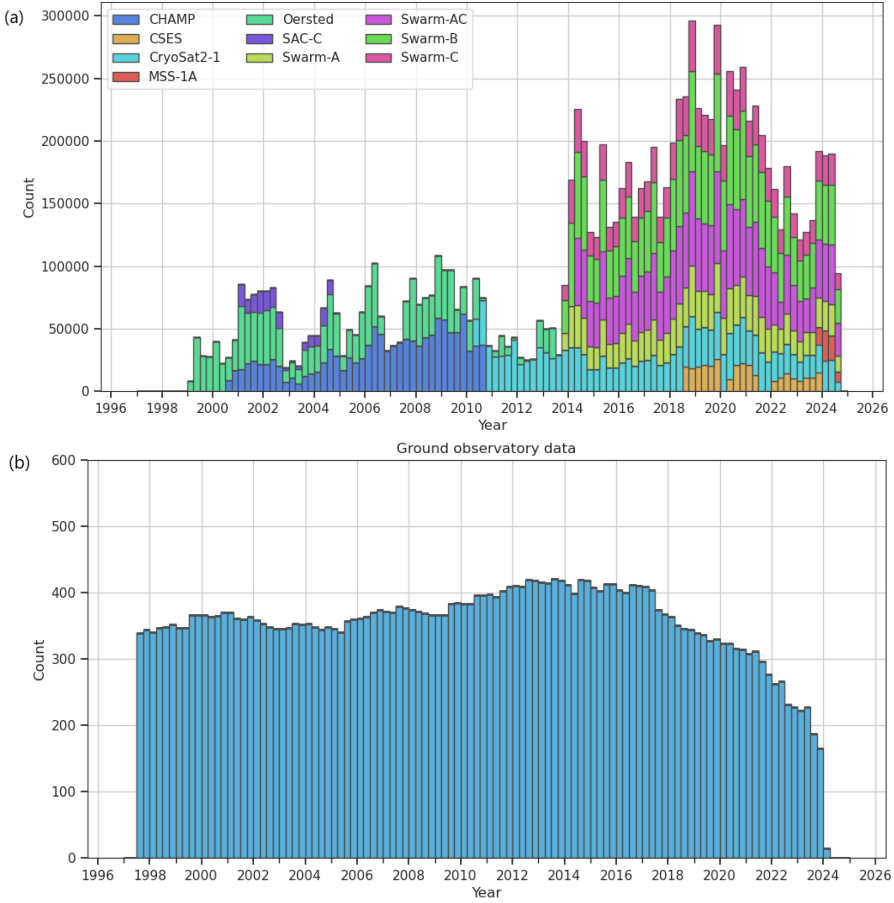


Figure 2: Stacked histograms of the amount of selected data in 3-month bins: (a) satellite data, (b) secular variation data from ground observatories. Swarm-AC refers to scalar and vector difference data between Swarm-A and Swarm-C.

with  $k = 6$  and using a uniform knot spacing of  $\Delta t_k = 0.5$  yr including a 6-fold endpoint multiplicity, covering the model time period from  $t_s = 1997.1$  to  $t_e = 2025.1$  in decimal years.

The small-scale internal field, for  $n \geq 21$ , is assumed static and the corresponding SH coefficients are therefore defined as constant in time.

### 3.1.2 Magnetospheric field

For the magnetospheric field, as for previous versions of the CHAOS model series, we adopt an expansion in the Solar Magnetic (SM) coordinate system in order to represent the field due to the ring-current in the inner magnetosphere ( $n \leq N_{\text{SM}}^{\text{mag}} = 2$ ) and an expansion in the GSM coordinate system in order to represent the field due to magnetopause and magnetotail currents in the outer magnetosphere ( $n \leq N_{\text{GSM}}^{\text{mag}} = 2$ , restricted to  $m = 0$  terms)

$$\begin{aligned}
 V^{\text{mag}}(t, r, \theta, \phi) = & a \sum_{n=1}^{N_{\text{SM}}^{\text{mag}}} \sum_{m=-n}^n \left(\frac{r}{a}\right)^n q_n^{m,\text{SM}}(t) Y_n^m(\theta_{\text{SM}}, \phi_{\text{SM}}) \\
 & + a \sum_{m=-1}^1 \hat{q}_1^{m,\text{SM}} \left[ RC_i(t) \left(\frac{a}{r}\right)^2 + RC_e(t) \left(\frac{r}{a}\right) \right] Y_1^m(\theta_{\text{SM}}, \phi_{\text{SM}}) \\
 & + a \sum_{n=1}^{N_{\text{GSM}}^{\text{mag}}} \left(\frac{r}{a}\right)^n q_n^{0,\text{GSM}} Y_n^0(\theta_{\text{GSM}}, \phi_{\text{GSM}}) \\
 & + \text{Earth-induced counterparts,}
 \end{aligned} \tag{5}$$

where  $\hat{q}_1^{m,\text{SM}}$  are constant regression coefficients multiplying the RC index,  $RC(t) = RC_e(t) + RC_i(t)$ , consisting of an external part  $RC_e$  and Earth-induced internal part  $RC_i$ . The degree-1 terms of  $q_n^{m,\text{SM}}$ , called RC baseline corrections, have an explicit time-dependence and are estimated in bins of  $\Delta t_{\text{SM}} = 30$  days, except for a single bin that is used during the gap period between May 2010 and April 2014. The degree-2 terms of  $q_n^{m,\text{SM}}$  and the

$q_n^{0,\text{GSM}}$  terms are assumed to be constant in time.

The use of magnetic coordinates allows an efficient parameterization of these sources, which have a slightly different geometry and temporal variation through the year. Definitions of the SM and GSM coordinate systems can be found, for example, in Laundal et al., 2017. The orientation of the geomagnetic dipole was fixed to IGRF-13 at epoch 2015 (Alken et al., 2021).

The Earth-induced counterparts of the time-varying magnetospheric field are based on the diagonal part of Q-matrices, derived from responses for an assumed 3D Earth conductivity model (Finlay et al., 2020; Grayver et al., 2017). These diagonal Q-matrices were also used for the separation of the  $RC$  index into external and Earth-induced parts.

### 3.1.3 Ionospheric field

In a significant change to previous version in the CHAOS model series, the parent model for IGRF-14 also includes a representation of the magnetic field produced by electrical currents flowing in the E-layer of the ionosphere, following the approach of the AMPS model (Laundal et al., 2018; Laundal et al., 2016). The ionospheric magnetic field is (and related large-scale induced fields) are represented by an internal scalar potential  $V^{\text{ion}}$ , because the E-layer currents flow below the satellite measurements used to constrain this part of the model. This internal scalar potential is expanded as

$$V^{\text{ion}}(t, r, \theta_{\text{QD}}, \phi_{\text{MLT}}) = a \sum_{n=1}^{N^{\text{ion}}} \sum_{\substack{m=-n \\ |m| \leq M^{\text{ion}}}}^n \left( \frac{a}{a + h_{\text{ref}}} \right)^{n+1} g_n^{m,\text{ion}}(t) Y_n^m(\theta_{\text{QD}}, \phi_{\text{MLT}}) \quad (6)$$

where  $h_{\text{ref}} = 110$  km is the chosen reference height for the QD coordinate system, coinciding with the approximate altitude of the highest electrical conductivity in the ionospheric E-layer. When computing the gradient of the potential to obtain the magnetic field  $\mathbf{B}^{\text{ion}}$ , the non-orthogonal basis vectors associated with the QD coordinate system, as defined by Laundal et al., 2017, are taken into account. The truncation degree and order were chosen to efficiently describe the magnetic field due to the electrojets in the polar region, where this parameterization is designed to work best.

In order to make use of the available information on the time-dependent solar driving of the E-layer currents, each spherical harmonic coefficient is further expanded as a sum of terms depending on various combinations of known external driving parameters

$$g_n^{m,\text{ion}}(t) = g_{n,0}^{m,\text{ion}} + \sum_{k=1}^{18} g_{n,k}^{m,\text{ion}} X_k(t), \quad (7)$$

where the  $X_k$  are given by

$$\begin{aligned} X_1 &= \sin \theta_c & X_2 &= \cos \theta_c & X_3 &= \epsilon & X_4 &= \epsilon \sin \theta_c & X_5 &= \epsilon \cos \theta_c & X_6 &= \beta_{\text{tilt}} \\ X_7 &= \beta_{\text{tilt}} \sin \theta_c & X_8 &= \beta_{\text{tilt}} \cos \theta_c & X_9 &= \epsilon \beta_{\text{tilt}} & X_{10} &= \epsilon \beta_{\text{tilt}} \sin \theta_c & X_{11} &= \epsilon \beta_{\text{tilt}} \cos \theta_c & X_{12} &= \tau \\ X_{13} &= \tau \sin \theta_c & X_{14} &= \tau \cos \theta_c & X_{15} &= \tau \beta_{\text{tilt}} & X_{16} &= \tau \beta_{\text{tilt}} \sin \theta_c & X_{17} &= \tau \beta_{\text{tilt}} \cos \theta_c & X_{18} &= F_{10.7}. \end{aligned} \quad (8)$$

with  $\beta_{\text{tilt}}$  the dipole tilt angle, parametrizing seasonal effects, given by

$$\beta_{\text{tilt}} = \arcsin(\hat{\mathbf{s}} \cdot \hat{\mathbf{m}}_{\text{dip}}), \quad (9)$$

where  $\hat{\mathbf{s}}$  is a unit vector in the direction of the sun and  $\hat{\mathbf{m}}_{\text{dip}}$  is the dipole moment of the IGRF magnetic field, and  $\tau$  the coupling function defined as

$$\tau = 10^{-3} v^{4/3} B_t^{2/3} \cos(\theta_c/2)^{8/3}, \quad (10)$$

which is similar to Newell's coupling function in Eq. 1 but maximizes for northward IMF, measuring the rate of lobe reconnection in the magnetotail. Further discussion and justifications for this form of expansion of the ionospheric field can be found in Laundal et al., 2018.

### 3.1.4 Magnetometer alignment and in-flight calibration

In addition to the field model parameters, we also co-estimated alignment parameters to rotate the observed vector field components from the magnetometer frame to the satellite body frame. The alignment parameters are written in terms of Euler angles  $\alpha$ ,  $\beta$ , and  $\gamma$  such that the magnetic field is given by

$$\mathbf{B}_{\text{CRF}} = \mathbf{R}_3(\gamma) \mathbf{R}_2(\beta) \mathbf{R}_1(\alpha) \mathbf{B}_{\text{VFM}} \quad (11)$$

where  $\mathbf{B}_{\text{CRF}}$  and  $\mathbf{B}_{\text{VFM}}$  are column vectors containing the vector components in the satellite body frame, also called the common reference frame (CRF), and the vector magnetometer frame (VFM), respectively. The rotation matrices  $\mathbf{R}_1$ ,  $\mathbf{R}_2$  and  $\mathbf{R}_3$  are given by

$$\mathbf{R}_1(\alpha) = \begin{pmatrix} 1 & 0 & 0 \\ 0 & \cos \alpha & -\sin \alpha \\ 0 & \sin \alpha & \cos \alpha \end{pmatrix}, \quad \mathbf{R}_2(\beta) = \begin{pmatrix} \cos \beta & 0 & \sin \beta \\ 0 & 1 & 0 \\ -\sin \beta & 0 & \cos \beta \end{pmatrix}, \quad \mathbf{R}_3(\gamma) = \begin{pmatrix} \cos \gamma & -\sin \gamma & 0 \\ \sin \gamma & \cos \gamma & 0 \\ 0 & 0 & 1 \end{pmatrix}. \quad (12)$$

In a final rotation, we transformed  $\mathbf{B}_{\text{CRF}}$  to spherical geocentric components, which can be related to the predictions of the field model, using the attitude information provided in the data product files.

Concerning CryoSat2-1, we co-estimated additional corrections of the platform magnetometer data, since these were produced using corrections and calibrations based on another field model. Our additional corrections are parameterized in the same way as an in-flight calibration, which relates the magnetic field in the VFM frame and the raw vector observations of the magnetometer, respectively written as column vectors  $\mathbf{B}_{\text{VFM}}$  and  $\mathbf{E}$ , according to

$$\mathbf{B}_{\text{VFM}} = \mathbf{P}^{-1} \mathbf{S}^{-1} (\mathbf{E} - \mathbf{b}). \quad (13)$$

In our case however,  $\mathbf{E}$  contains the pre-corrected and pre-calibrated platform magnetometer data in nT provided in the CryoSat2 data files. The other vectors and matrices appearing in Eq. 13 are

$$\mathbf{b} = \begin{bmatrix} b_1 \\ b_2 \\ b_3 \end{bmatrix}, \quad \mathbf{S} = \begin{bmatrix} s_1 & 0 & 0 \\ 0 & s_2 & 0 \\ 0 & 0 & s_3 \end{bmatrix}, \quad \mathbf{P} = \begin{bmatrix} 1 & 0 & 0 \\ -\sin u_1 & \cos u_1 & 0 \\ \sin u_2 & \sin u_3 & \sqrt{1 - \sin^2 u_2 - \sin^2 u_3} \end{bmatrix}, \quad (14)$$

where  $(b_1, b_2, b_3)$  are the component biases,  $(s_1, s_2, s_3)$  are the scale factors, and  $(u_1, u_2, u_3)$  are the non-orthogonality angles.

We estimated alignment (and for Cryosat-2 also calibration correction parameters), for each satellite dataset separately in bins of 30 days. Only data for dark conditions were used to estimate the alignment parameters, except for the case of CryoSat2-1 data, where data on both day and nightside were used to estimate the alignment and calibration correction parameters.

### 3.2 Model estimation

We collect the field model parameters in the column vector  $\mathbf{p}$ , the alignment parameters in  $\mathbf{q}$ , and the calibration parameters in  $\mathbf{c}$ , and combine these into a single model parameter vector  $\mathbf{m} = [\mathbf{p}; \mathbf{q}; \mathbf{c}]$ . Model parameters were then estimated by minimizing the quadratic cost function

$$\Phi(\mathbf{m}) = [\mathbf{d}(\mathbf{q}, \mathbf{c}) - \mathbf{g}(\mathbf{p})]^T \mathbf{C}_d^{-1} [\mathbf{d}(\mathbf{q}, \mathbf{c}) - \mathbf{g}(\mathbf{p})] + \mathbf{m}^T \mathbf{R} \mathbf{m} \quad (15)$$

where  $\mathbf{g}(\mathbf{p})$  is the vector of magnetic field predictions that depend on the field model parameters,  $\mathbf{C}_d$  is the data error covariance matrix including robust weighting (see Sect. 3.2.1),  $\mathbf{d}(\mathbf{q}, \mathbf{c})$  is the data vector that depends on alignment parameters (and calibration correction parameters in the case of Cryosat-2), and  $\mathbf{R}$  is the model regularization matrix (see Sect. 3.2.2).

Minimizing this cost function is a non-linear problem due to the presence of scalar data, robust weighting, alignment, and calibration correction parameters. Since it is only mildly non-linear, the problem can be linearized and the solution sought through an iterative procedure involving the partial derivatives of the cost function. The model parameters were updated each iteration according to

$$\mathbf{m}_{i+1} = \mathbf{m}_i + (\mathbf{G}_i^T \mathbf{C}_d^{-1} \mathbf{G}_i + \mathbf{R})^{-1} \{ \mathbf{G}_i^T \mathbf{C}_d^{-1} [\mathbf{d}(\mathbf{q}_i, \mathbf{c}_i) - \mathbf{g}(\mathbf{p}_i)] - \mathbf{R} \mathbf{m}_i \} \quad (16)$$

where  $\mathbf{G}_i$  is the partial derivative of the residuals  $\mathbf{d}(\mathbf{q}, \mathbf{c}) - \mathbf{g}(\mathbf{p})$  with respect to the model parameters and is evaluated using the model parameters  $\mathbf{m}_i$  from the previous iteration. As the starting model  $\mathbf{m}_0$  for the iterative minimization, we used the CHAOS-7.18 model, linearly extrapolated to the most recent satellite data, to initialize the internal field while setting the magnetospheric and ionospheric fields to zero. Initial parameter values for the Euler angles were taken from results obtained during pre-flight calibration on ground for CHAMP (Schwintzer et al., 2002) and the *Swarm* satellites (Tøffner-Clausen et al., 2019), and through in-flight calibration for CryoSat2 (Olsen et al., 2020) and the MSS-1A satellite. Concerning the initial values for the CryoSat2-1 correction parameters, we used zero-valued biases and non-orthogonality angles, and unit sensitivities.

To avoid the effect of remaining dayside ionospheric signals on the estimation of the model parameters for the internal field, magnetospheric field, and alignment parameters, we modified  $\mathbf{G}$  such that the entries with row indices associated with sunlit data were zero, except if they also have column indices associated with the ionospheric field and CryoSat2-1 correction parameters. In other words, the sunlit data was only used to estimate the ionospheric field and CryoSat2-1 correction parameters of the model, while the dark data was

used to constrain all model parts. In addition, entries related to  $g_1^0$  B-spline coefficients and the platform magnetometer data were set to zero to reduce cross-talk between the axial dipole coefficient of the internal field and the CryoSat2-1 sensitivity parameters.

The model was considered converged when the model parameters, which contain the geophysical information of interest, changed only slightly between successive iterations. We used a convergence criterion based on the relative change of the model parameters

$$\frac{||\mathbf{m}_{i+1} - \mathbf{m}_i||}{||\mathbf{m}_i||} < 1 \times 10^{-6}, \quad (17)$$

which was reached after 15 iterations.

### 3.2.1 Data error covariances

The data error covariance matrix contains the estimated data error variances for each satellite dataset and for each type of data, i.e. vector, scalar, field differences etc. For the vector data, we specified the error variances with respect to the bore-sight direction of the star cameras onboard the satellite to account for anisotropic errors due to imprecise attitude information. Following Holme et al., 1996, the data errors can be written in terms of an isotropic instrument error  $\sigma$ , a bore-sight pointing error  $\psi$ , and a rotation error  $\chi$  about the bore-sight direction. This treatment is particularly important for the vector data from the Ørsted satellite, where the pointing and rotation errors are different. Concerning the scalar, scalar difference and vector difference data, we specified the expected standard deviations  $\sigma_F$ ,  $\sigma_{\delta F}$ , and  $\sigma_{\delta B}$ , respectively. Tab. 3 summarizes the chosen a-priori data errors for the various data types. The error estimates for the ground observatory SV data were

Table 3: Adopted errors for the satellite data. Subscripts  $F$ ,  $\delta B$  and  $\delta F$  refer to scalar, vector difference, and scalar difference data, respectively.

Dataset	$\sigma$ (nT)	$\psi$ (arcsec)	$\chi$ (arcsec)	$\sigma_F$ (nT)	$\sigma_{\delta F}$ (nT)	$\sigma_{\delta B}$ (nT)
Ørsted	2.5	10	40 <sup>†</sup>	2.5	0.4	n.a.
CHAMP	2.5	10	10	2.5	0.4	0.4
CryoSat2-1	6.0	30	30	6.0	n.a.	n.a.
MSS-1A	2.2	5	5	n.a.	n.a.	n.a.
CSES	n.a.	n.a.	n.a.	2.5	n.a.	n.a.
SAC-C	n.a.	n.a.	n.a.	2.5	n.a.	n.a.
Swarm-A	2.2	5	5	2.2	0.4	0.4
Swarm-B	2.2	5	5	2.2	0.4	0.4
Swarm-C	2.2	5	5	2.2	0.4	0.4
Swarm-AC	n.a.	n.a.	n.a.	n.a.	0.4	0.4

<sup>†</sup> Increases to 60 arcsec for data after 24th January 2000.

derived from residuals to a preliminary version of the DTU parent model, taking into account the covariances between the vector components.

Finally, to account for the expected long-tailed error distributions, we employed an iterative data re-weighting approach based on robust Huber weights (Huber, 2004). Additional data weighting based on  $\sin \theta$  was also applied to balance the larger amount of data collected at polar latitudes, for the satellites with high-inclination orbits.

### 3.2.2 Model regularization

Imperfect data distribution and unmodeled signals in the data can adversely effect the quality of geomagnetic field models; regularization is a commonly used tool to handle such issues. Here, we applied specific model regularizations to each part of our parent mode. The implemented model regularization matrix  $\mathbf{R}$  is therefore block-diagonal, with the entries of each sub-matrix implementing a quadratic norm penalizing the temporal or spatial complexity of a specific aspect of the model. To control the strength of these regularizations, the quadratic norms are scaled by strictly positive regularization parameters that are chosen before estimating the model parameters. Tab. 4 collects the numerical values of these regularization parameters. A brief description of the regularization norms implemented for each part of the model is given below.

Temporal regularization of the time-dependent internal field was implemented in two ways. First, we regularized the acceleration of the internal field throughout the model timespan based on an a-priori model covariance

Table 4: Choice of regularization parameters.

Regularization parameter	Value
$t_s$	$0.01 \text{ (nT/yr}^2\text{)}^{-2}$
$t_e$	$0.01 \text{ (nT/yr}^2\text{)}^{-2}$
$\lambda_{\text{SM}}$	$1500 \text{ (nT/yr)}^{-2}$
$\lambda_b$	$160 \text{ (nT/yr)}^{-2}$
$\lambda_s$	$1.6 \times 10^{10} \text{ (1/yr)}^{-2}$
$\lambda_u$	$1.6 \times 10^5 \text{ (rad/yr)}^{-2}$
$\lambda_{\text{ion}}$	$5 \times 10^4 \text{ (nT)}^{-2}$

matrix for the field acceleration, obtained from state-of-the-art geodynamo simulations. No regularization parameter was used to scale this new physics-based regularization of the field acceleration. In addition, at the model endpoints  $t_s$  and  $t_e$ , we further regularized the squared acceleration of the internal radial field integrated over the core surface, scaling this using a regularization parameter  $\lambda_e^{\text{int}} = \lambda_s^{\text{int}} = 0.01 \text{ (nT/yr}^2\text{)}^{-2}$ . No special treatment of the zonal terms, or high degree tapering was needed in this regularization of the internal field.

The a-priori regularization of the field acceleration is based on statistical information obtained from the 71p (Aubert et al., 2021) and 100p (Aubert, 2023) versions of the coupled-Earth geodynamo simulation, in which field variations and accelerations (including geomagnetic jerks) are driven by both convective and hydromagnetic wave processes (Aubert et al., 2019, 2022). Long time series of simulated spherical harmonic coefficients of the field acceleration were fit by a stochastic process model (an auto-regressive process of order 3) using a maximum likelihood method (Gillet et al., 2024; Lütkepohl, 2005). Many realizations of the resulting stochastic processes were then used to construct a well-behaved spatio-temporal prior model covariance matrix for the field acceleration. We retained only the temporal covariances and discarded the cross-covariances between different spherical harmonics as these could depend sensitively on the simulation setup. Finally, we inverted this a-priori model temporal covariance matrix for the field acceleration and projected it onto the spline basis of our time-dependent internal model to obtain a suitable block of the model regularization matrix  $\mathbf{R}$ .

Besides the internal field, we also regularized the average of the squared bin-to-bin difference for various parts of the model to control their temporal variability. This type of regularization was applied to the  $RC$ -baseline corrections, scaled by  $\lambda_{\text{SM}} = 1500 \text{ (nT/yr)}^{-2}$ ; and the biases, sensitivities and non-orthogonality angles for CryoSat2-1, respectively scaled by  $\lambda_b = 160 \text{ (nT/yr)}^{-2}$ ,  $\lambda_s = 1.6 \times 10^{10} \text{ (1/yr)}^{-2}$ , and  $\lambda_u = 1.6 \times 10^5 \text{ (rad/yr)}^{-2}$ .

Concerning the ionospheric field, we implemented a regularization norm  $R^{\text{ion}}(\mathbf{m})$  based on the squared value of the time-averaged radial magnetic field at an altitude of  $h = 100 \text{ km}$ , integrated over the sphere in QD/MLT coordinates,

$$R^{\text{ion}}(\mathbf{m}) = \frac{1}{4\pi} \int_0^\pi \int_0^{2\pi} \langle B_r^{\text{ion}}(\mathbf{m}; r = a + h_{\text{ref}}, \theta_{\text{QD}}, \phi_{\text{MLT}}) \rangle^2 \sin \theta_{\text{QD}} d\phi_{\text{MLT}} d\theta_{\text{QD}} \quad (18)$$

where  $\langle \cdot \rangle$  denotes the average over the model time period. The computation of the time-average of the ionospheric magnetic field involves the average values of the external driving parameters in Eq. (8), which we obtained before estimating the model by forming the arithmetic mean of the driving parameters for the times of the selected scalar and vector data. The regularization norm was scaled by  $\lambda_{\text{ion}} = 5 \times 10^4 \text{ (nT)}^{-2}$ . Low-degree terms ( $n \leq 7$ ) are furthermore regularized 10 times stronger than higher-degree terms ( $n \geq 13$ ) with a smooth transition between these levels using a cosine taper. This regularization penalizes the large-scale time-average of the radial ionospheric field in the QD/MLT coordinate frame. It strongly affects the ionospheric model parameters associated with external driving parameters that have large non-zero baseline values. However, since only the time-average is regularized, the ionospheric field can still vary in time according to the time variations in the external driving. If the average ionospheric field is not regularized, large non-zero baselines of the external driving parameters can adversely affect the estimated internal field, especially the zonal and near-zonal terms at low SH degrees in geographic coordinates. We chose the value of the regularization parameter to minimize these low SH degree artifacts, while permitting the ionospheric field to have a non-zero, but small, time average.

## 4 Results from the DTU parent model

### 4.1 Fit to the satellite data

Tab. 5 – 14 show misfit statistics for the selected satellite data during dark conditions.

Table 5: Model statistics of misfit between the DTU parent model and the Ørsted data during dark conditions. Mean and RMS refer to Huber-weighted mean and RMS values.  $\delta F$  denotes scalar difference data.

Dataset	QD latitude	Component	N	Mean (nT)	RMS (nT)
Ørsted	non-polar	$B_r$	46629	-0.06	3.92
		$B_\theta$	46629	-0.03	4.69
		$B_\phi$	46629	-0.02	4.61
		$F$	215810	0.59	2.13
	polar	$\delta F$	132248	0.00	0.21
		$F$	133603	0.86	2.88
		$\delta F$	62129	0.00	0.34

Table 6: Model statistics of misfit between the DTU parent model and the CHAMP data during dark conditions. Mean and RMS refer to Huber-weighted mean and RMS values.  $\delta F$  denotes scalar difference data and  $\delta \mathbf{B}$  vector difference data.

Dataset	QD latitude	Component	N	Mean (nT)	RMS (nT)
CHAMP	non-polar	$B_r$	225911	0.09	1.80
		$B_\theta$	225911	0.25	2.41
		$B_\phi$	225911	-0.04	2.12
		$\delta B_r$	110757	0.00	0.40
	polar	$\delta B_\theta$	110757	-0.01	0.40
		$\delta B_\phi$	110757	-0.00	0.43
		$\delta F$	144175	0.00	0.28
		$F$	120472	-0.98	3.72
		$\delta F$	72089	-0.00	0.72

Table 7: Model statistics of misfit between the DTU parent model and the SAC-C data during dark conditions. Mean and RMS refer to Huber-weighted mean and RMS values.

Dataset	QD latitude	Component	N	Mean (nT)	RMS (nT)
SAC-C	non-polar	$F$	46147	0.22	2.37
		$F$	25337	0.30	3.15

Table 8: Model statistics of misfit between the DTU parent model and the CryoSat2-1 data during dark conditions. Mean and RMS refer to Huber-weighted mean and RMS values.

Dataset	QD latitude	Component	N	Mean (nT)	RMS (nT)
CryoSat2-1	non-polar	$B_r$	403686	-0.10	3.03
		$B_\theta$	403686	0.13	4.02
		$B_\phi$	403686	-0.11	3.40
	polar	$F$	220038	-1.24	4.38

Table 9: Model statistics of misfit between the DTU parent model and the Swarm-A data during dark conditions. Mean and RMS refer to Huber-weighted mean and RMS values.  $\delta F$  denotes scalar difference data and  $\delta \mathbf{B}$  vector difference data.

Dataset	QD latitude	Component	N	Mean (nT)	RMS (nT)
Swarm-A	non-polar	$B_r$	152087	0.07	1.40
		$B_\theta$	152087	0.09	2.19
		$B_\phi$	152087	-0.04	1.92
		$\delta B_r$	74903	-0.00	0.24
		$\delta B_\theta$	74903	-0.00	0.24
		$\delta B_\phi$	74903	-0.00	0.33
		$\delta F$	95878	-0.00	0.14
	polar	$F$	81392	-0.17	3.16
		$\delta F$	48223	-0.00	0.56

Table 10: Model statistics of misfit between the DTU parent model and the Swarm-B data during dark conditions. Mean and RMS refer to Huber-weighted mean and RMS values.  $\delta F$  denotes scalar difference data and  $\delta \mathbf{B}$  vector difference data.

Dataset	QD latitude	Component	N	Mean (nT)	RMS (nT)
Swarm-B	non-polar	$B_r$	299843	-0.03	1.38
		$B_\theta$	299843	0.02	2.15
		$B_\phi$	299843	-0.05	1.90
		$\delta B_r$	147742	0.00	0.23
		$\delta B_\theta$	147742	-0.00	0.23
		$\delta B_\phi$	147742	-0.00	0.33
		$\delta F$	189832	-0.00	0.12
	polar	$F$	160064	0.00	3.00
		$\delta F$	95729	-0.00	0.49

Table 11: Model statistics of misfit between the DTU parent model and the Swarm-C data during dark conditions. Mean and RMS refer to Huber-weighted mean and RMS values.  $\delta F$  denotes scalar difference data and  $\delta \mathbf{B}$  vector difference data.

Dataset	QD latitude	Component	N	Mean (nT)	RMS (nT)
Swarm-C	non-polar	$B_r$	152569	0.09	1.42
		$B_\theta$	152569	0.02	2.19
		$B_\phi$	152569	-0.06	1.95
		$\delta B_r$	75153	-0.00	0.25
		$\delta B_\theta$	75153	-0.00	0.25
		$\delta B_\phi$	75153	0.00	0.34
		$\delta F$	96264	-0.00	0.15
	polar	$F$	81567	-0.12	3.16
		$\delta F$	48339	-0.00	0.55

Table 12: Model statistics of misfit between the DTU parent model and the data obtained by differencing Swarm-A and Swarm-C data during dark conditions. Mean and RMS refer to Huber-weighted mean and RMS values.  $\delta F$  denotes scalar difference data and  $\delta \mathbf{B}$  vector difference data.

Dataset	QD latitude	Component	N	Mean (nT)	RMS (nT)
Swarm-AC	non-polar	$\delta B_r$	282254	0.03	0.53
		$\delta B_\theta$	282254	-0.06	0.62
		$\delta B_\phi$	282254	-0.00	0.58
		$\delta F$	359269	0.03	0.41
	polar	$\delta F$	184563	0.07	0.46

Table 13: Model statistics of misfit between the DTU parent model and the CSES data during dark conditions. Mean and RMS refer to Huber-weighted mean and RMS values.

Dataset	QD latitude	Component	N	Mean (nT)	RMS (nT)
CSES	non-polar	$F$	122876	0.65	1.85
	polar	$F$	18396	1.86	3.13

Table 14: Model statistics of misfit between the DTU parent model and the MSS-1A data during dark conditions. Mean and RMS refer to Huber-weighted mean and RMS values.

Dataset	QD latitude	Component	N	Mean (nT)	RMS (nT)
MSS-1A	non-polar	$B_r$	28739	-0.08	1.76
		$B_\theta$	28739	0.10	2.87
		$B_\phi$	28739	-0.01	2.51

## 4.2 Fit to the ground observatory data

Tab. 15 shows the misfit statistics for the annual differences of revised monthly means from ground observatory data.

Table 15: Model statistics of misfit between the DTU parent model and the ground observatory SV data. Mean and RMS refer to Huber-weighted mean and RMS values.

Dataset	QD latitude	Component	N	Mean (nT/yr)	RMS (nT/yr)
Observatory	non-polar	$\dot{B}_r$	28392	0.10	2.57
		$\dot{B}_\theta$	28392	-0.13	2.51
		$\dot{B}_\phi$	28392	0.05	2.83
	polar	$\dot{B}_r$	9571	-0.06	6.23
		$\dot{B}_\theta$	9571	-0.21	5.18
		$\dot{B}_\phi$	9571	-0.10	4.12

Fig. 3 shows time series of contributing SV data for example ground observatories, compared to the SV estimates from the DTU parent model.

## 4.3 Spherical harmonic power spectra of the internal field

Fig. 4 shows the spherical harmonic power spectra for our IGRF-2025 candidate and the SV-2025-2030 candidate at the Earth's surface, compared to CHAOS-7.18 and IGRF-13 (Alken et al., 2021).

Fig. 5 shows the spherical harmonic power spectrum of the SV from the DTU parent model for different years, compared to CHAOS-7.18.

Fig. 6 shows the spherical harmonic power spectrum of the SA from the DTU parent model for different years, compared to CHAOS-7.18.

## 4.4 Time-dependence of SV coefficients

Fig. 7 shows time series of SV coefficients for  $n \leq 8$  for the DTU parent model, CHAOS-7.18 and our candidate for the average predictive SV between 2025 and 2030.

## 4.5 Co-estimated ionospheric field

Fig. 8 shows an example of the modeled ionospheric field at satellite altitude at UT noon during northern summer. Here, the ionospheric field is shown for slightly more active conditions compared to those present in the quiet-time selected data used during the modeling. The distinctive two-cell pattern of the ionospheric field, visible in the northern polar region during northern summer, is therefore more pronounced in this example than is expected for quiet-time conditions.

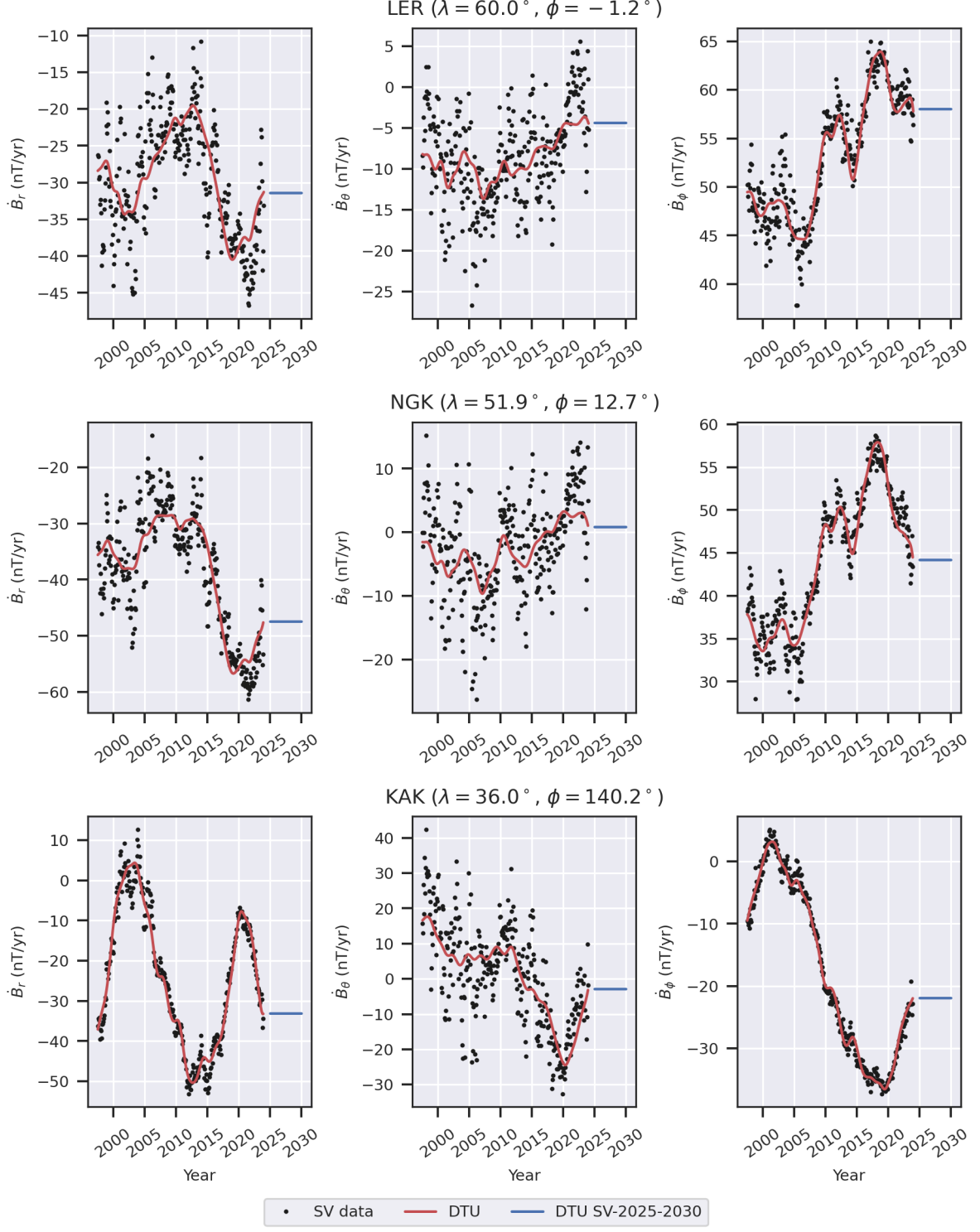


Figure 3: Time series of SV data, i.e. annual differences of revised monthly means, for example ground observatories (black dots). The red lines show the SV estimates from the DTU parent model and the blue lines are our candidate for the SV-2025-2030.

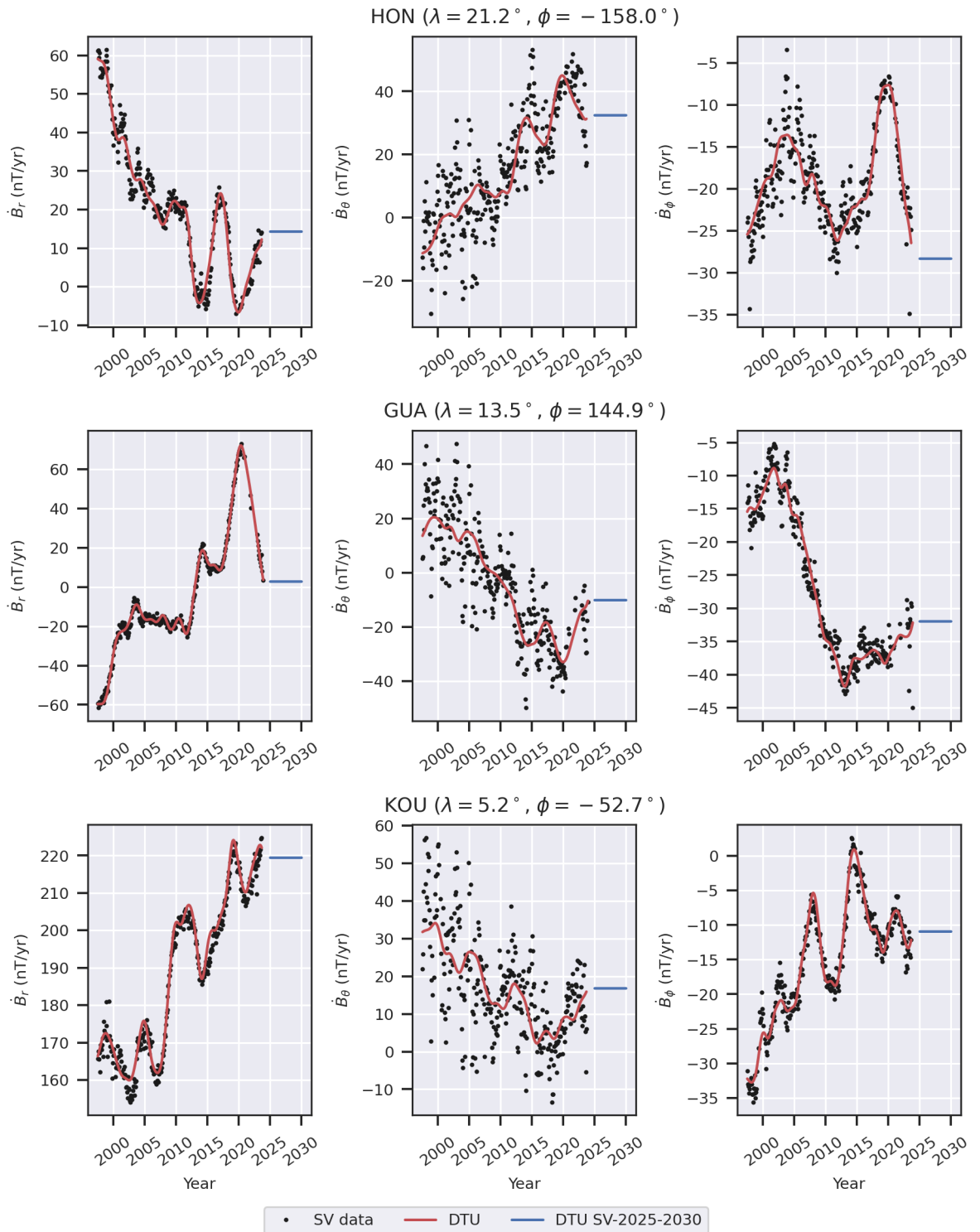


Figure 3 (cont.)

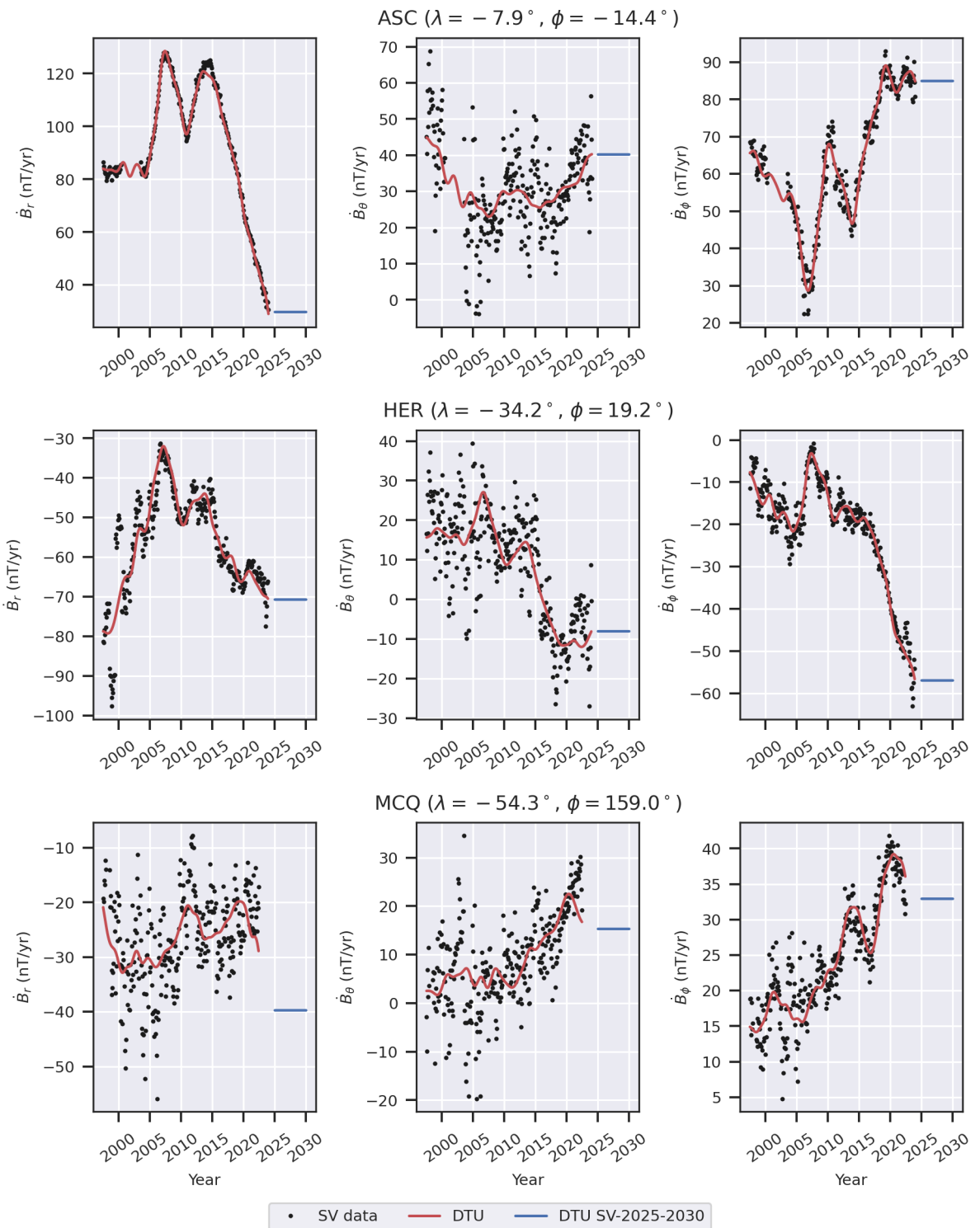


Figure 3 (cont.)

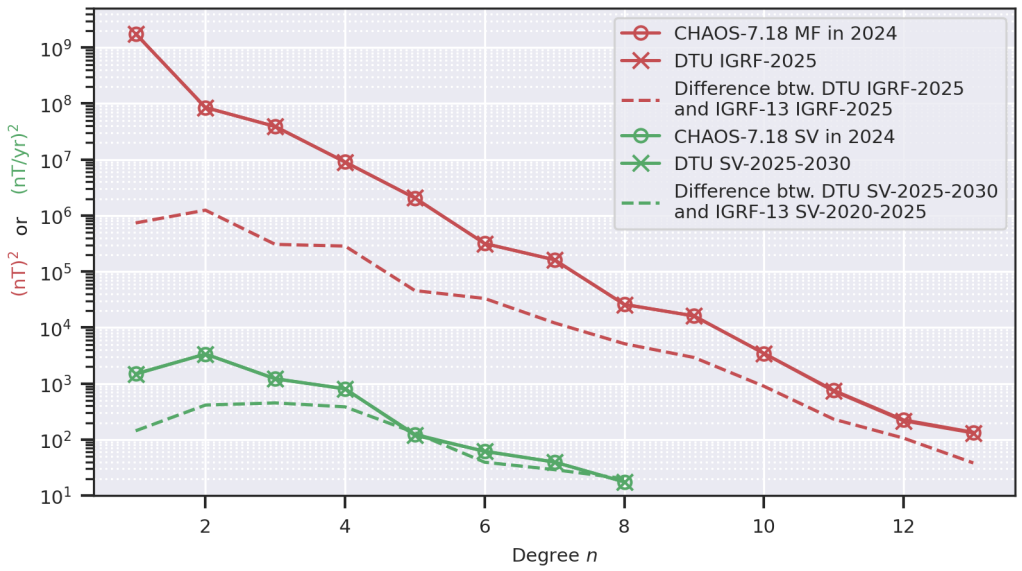


Figure 4: Spherical harmonic power spectra at the Earth’s surface. The spectra of the mean square vector magnetic field for  $n \leq 13$  (red line with circles) and it’s first time derivative for  $n \leq 8$  (SV, green line with circles) are shown for CHAOS-7.18 in 2024.0. DTU IGRF-2025 (red line with crosses) and its difference with IGRF-13 IGRF-2025 (dashed red line) are shown, as well as DTU SV-2025-2030 (green line with crosses) and its difference with IGRF-13 SV-2020-2025 (dashed green line).

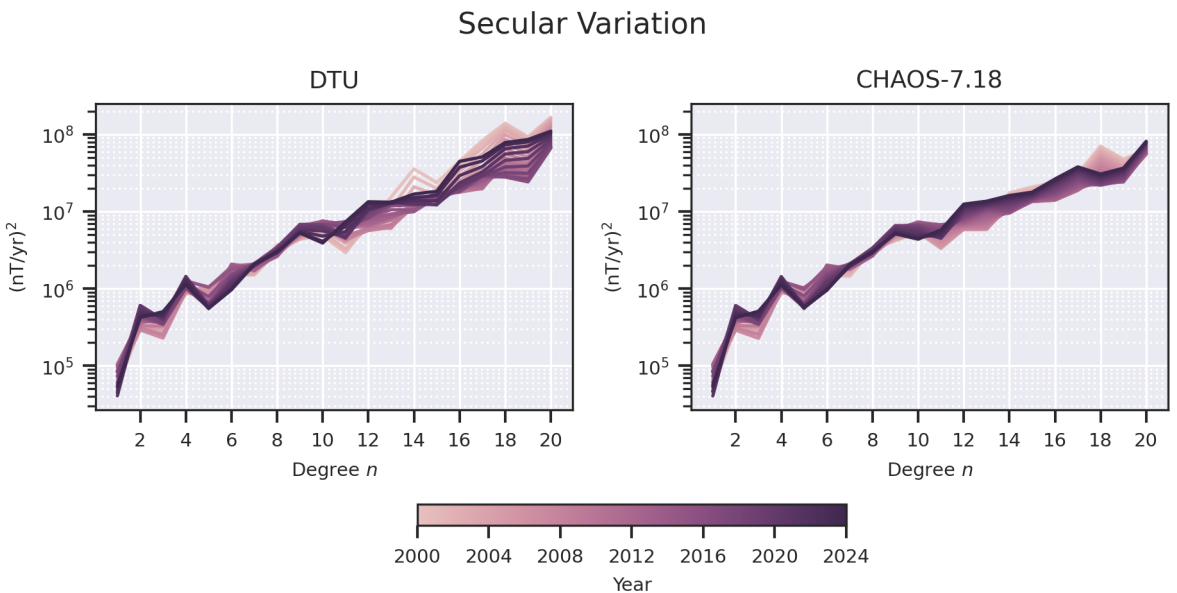


Figure 5: Spherical harmonic power spectra of the mean squared SV at the Earth’s core for different years. The left panel shows the DTU parent model and the right panel shows CHAOS-7.18.

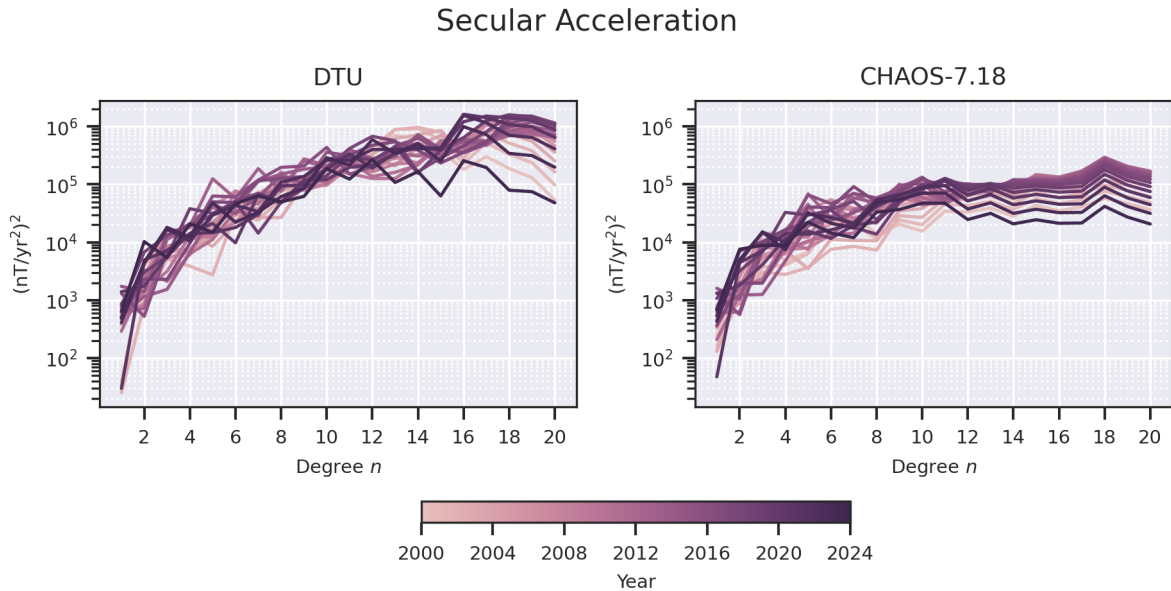


Figure 6: Spherical harmonic power spectra of the mean squared secular acceleration at the Earth's core for different years. The left panel shows the DTU parent model and the right panel shows CHAOS-7.18.

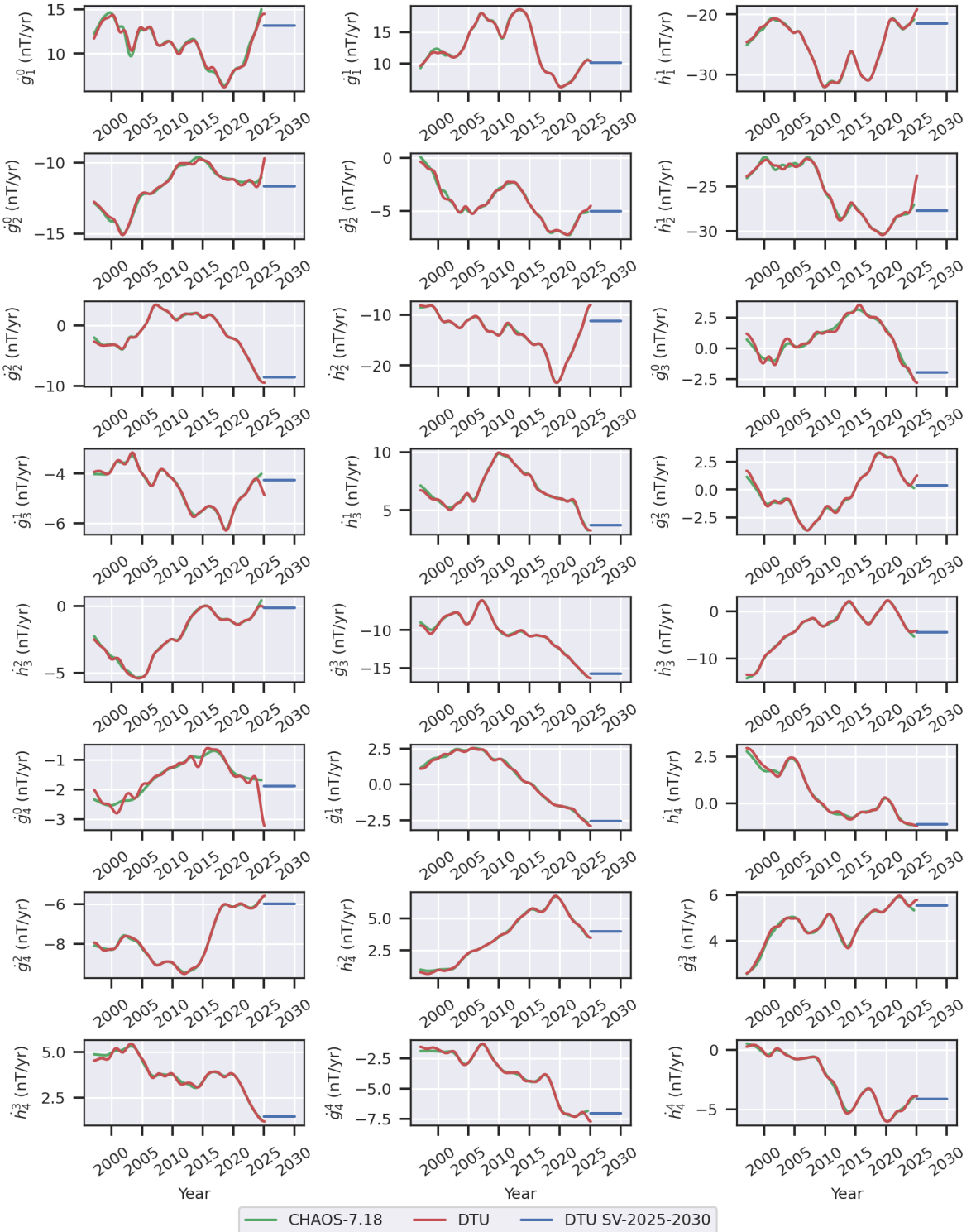


Figure 7: Time series of SV coefficients for  $n \leq 8$ . The panels show the DTU parent model (red), CHAOS-7.18 (green), and the our candidate for the average predictive SV (blue) for the 2025–2030 time period.

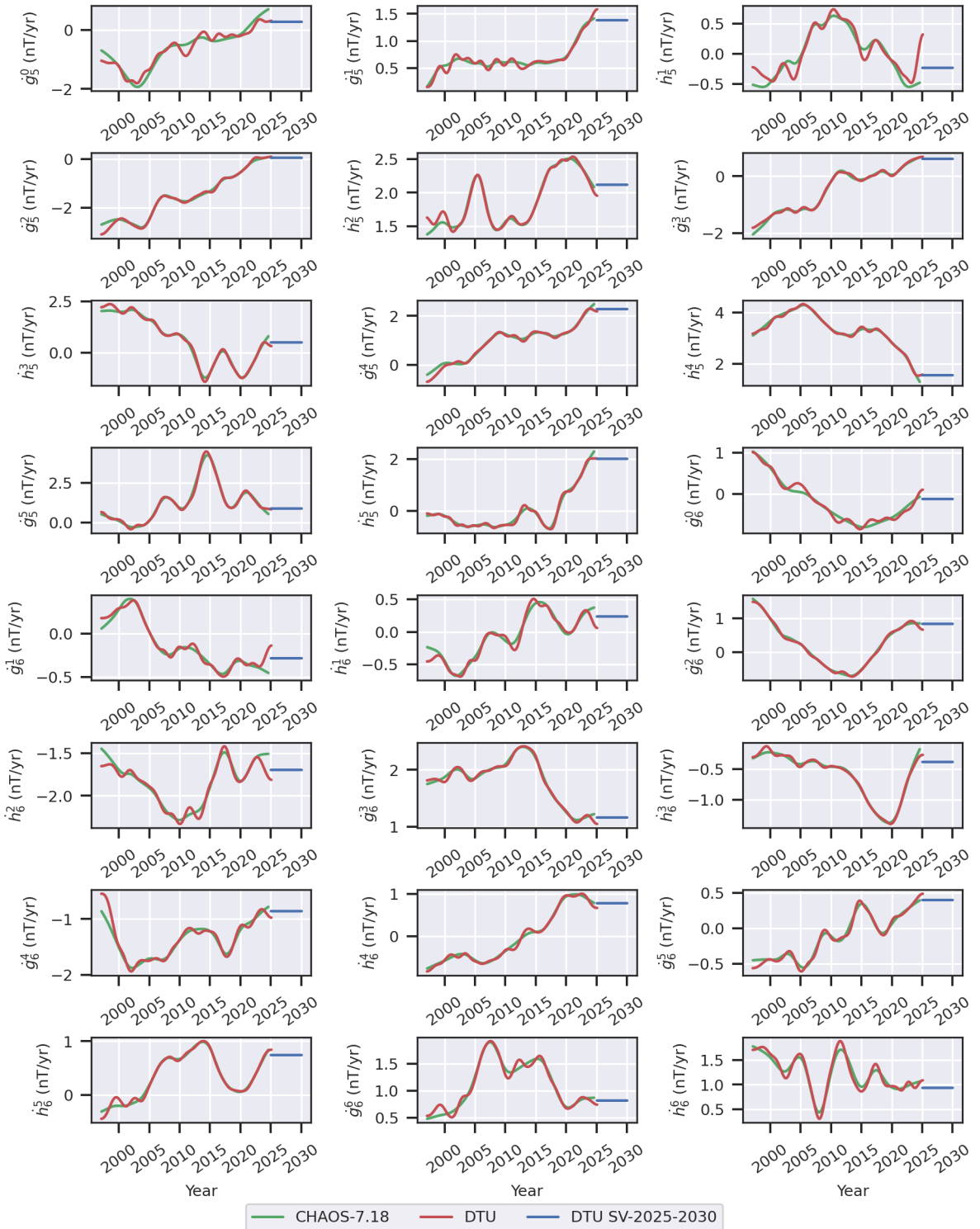


Figure 7 (cont.)

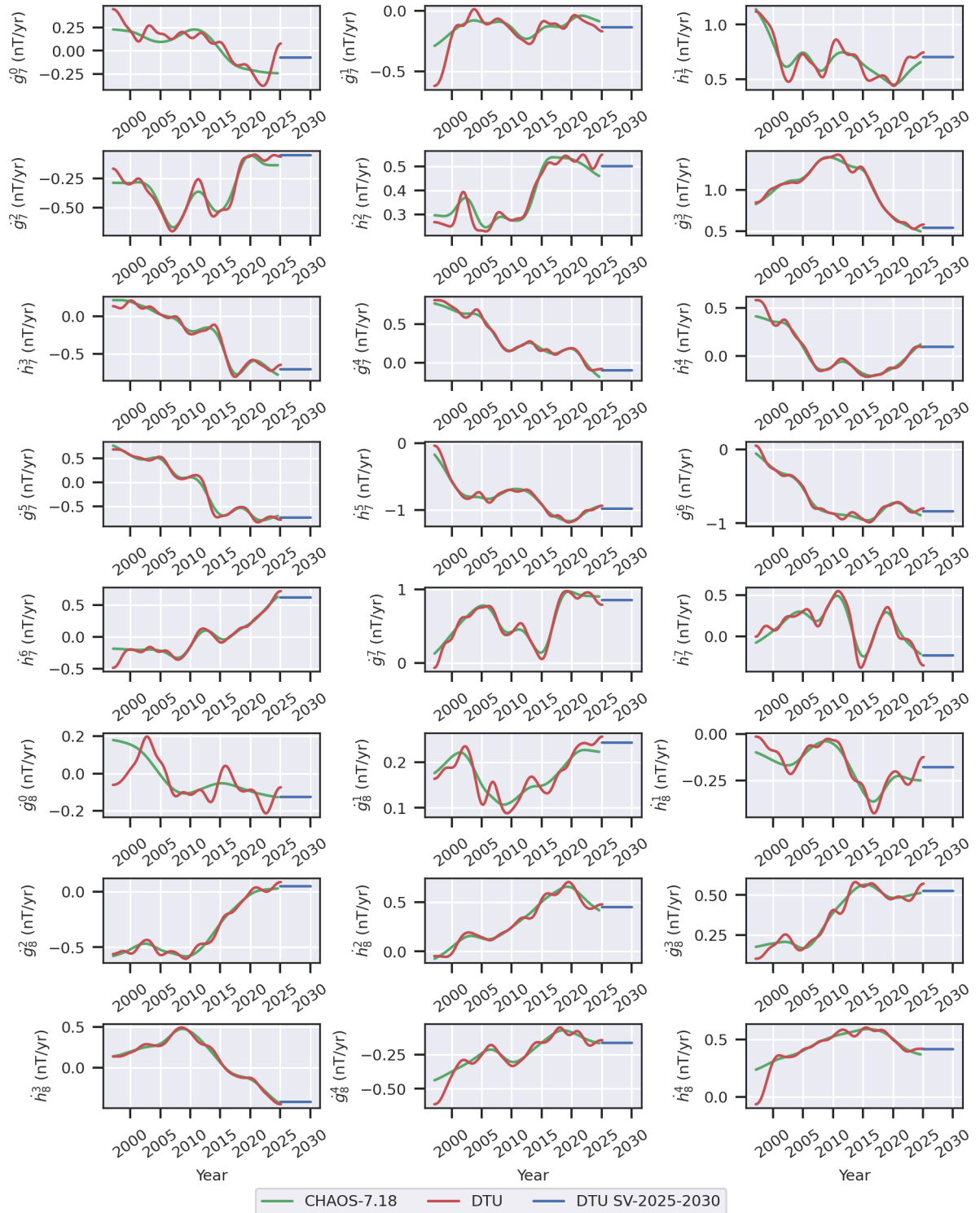


Figure 7 (cont.)

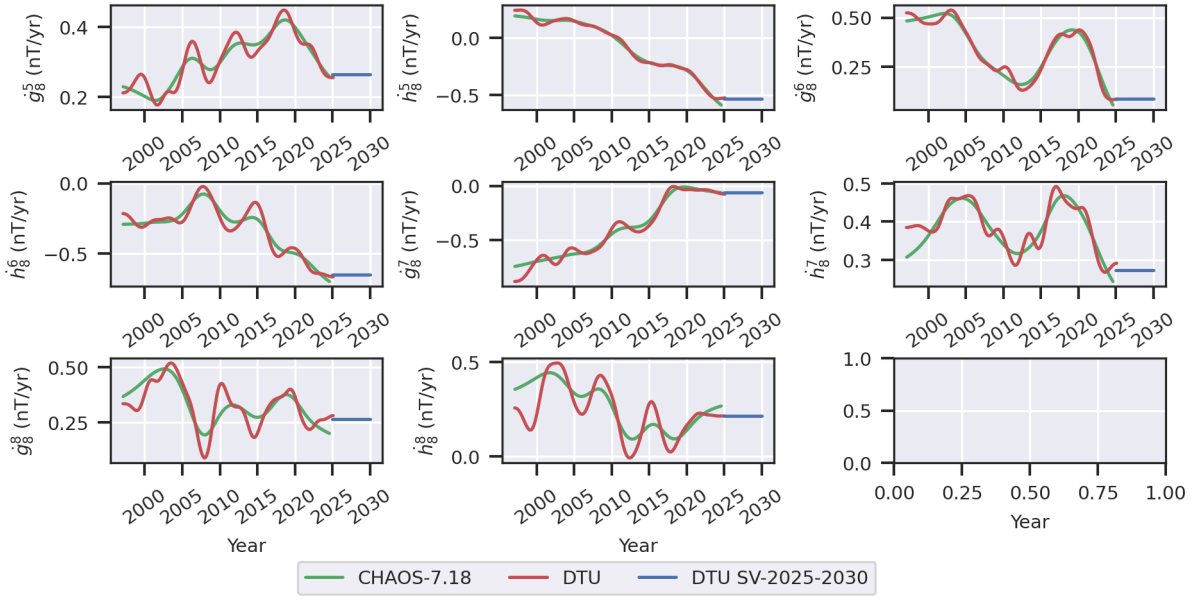


Figure 7 (cont.)

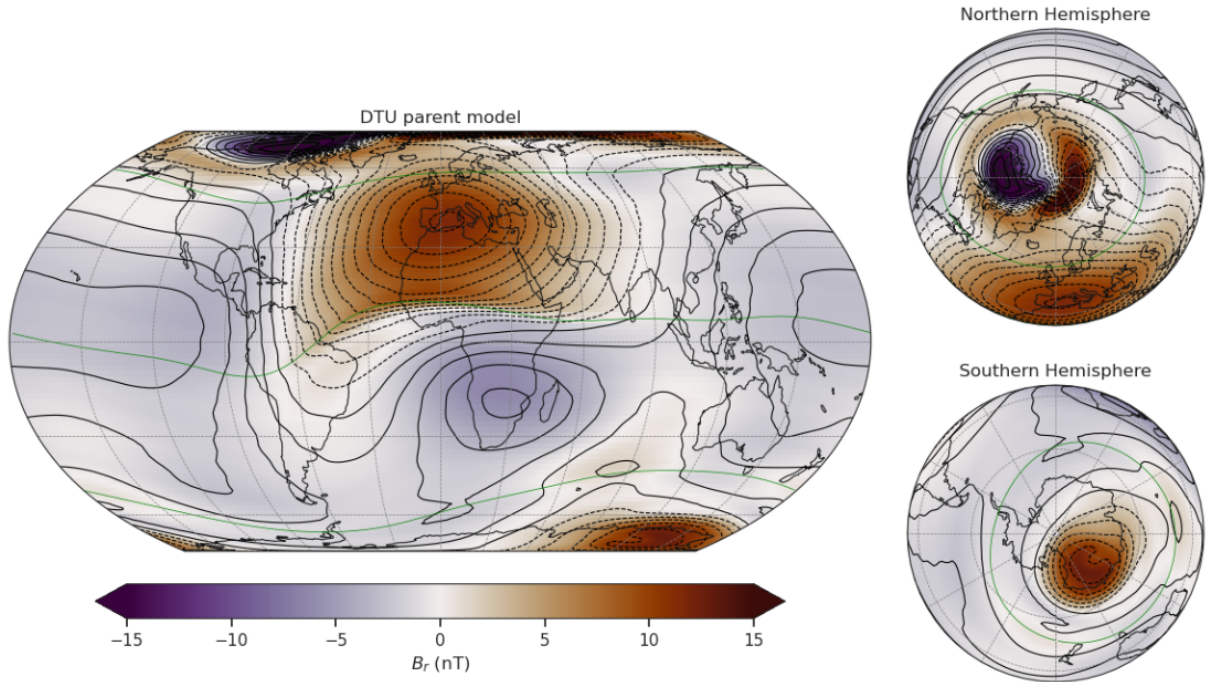


Figure 8: Example of the radial component of the ionospheric field from the DTU parent model at 450 km altitude for  $n \leq 45$  at UT noon during northern summer. In this example, we illustrate the ionospheric currents for a case when  $B_{\text{IMF},z}$  is negative, which involves more active geomagnetic conditions than those allowed by the strict quiet-time selection criteria employed during the field modeling. More specifically, the external driving parameters are set to values of  $\theta_c = 160^\circ$ ,  $B_t = 2$  nT, and solar wind speed  $v = 350$  km s $^{-1}$  and  $F_{10.7} = 70$  sfu. Green lines indicate magnetic latitudes at  $-55^\circ$ ,  $0^\circ$ , and  $55^\circ$ . Black lines are stream lines at 5 kA intervals of the predicted divergence-free horizontal sheet current in the ionospheric E-layer at 110 km altitude.

## 5 Extraction of DTU's candidate models for IGRF-14

Details on the extraction of our candidate models for the DGRF-2020, IGRF-2025, and the average predicted SV are given below. No model uncertainty estimates were provided. We expect largest errors are biases due to imperfectly modeled external and induced signals, which are not very well captured when one simply computes the formal model error covariance matrix.

### 5.1 DGRF-2020

To extract the DGRF-2020 candidate, we evaluated the internal field of our parent model, which has a B-spline based time-dependence, at epoch 2020.0 up to degree and order 13 in nT with a numerical precision of 0.01 nT.

### 5.2 IGRF-2025

For the IGRF-2025 candidate, we evaluated the spline-based internal field of our parent model at epoch 2024.75, and linearly propagated the obtained coefficients forward to epoch 2025.0 using the SV predicted by our parent model at epoch 2024.0

$$g_n^m(t = 2025.0) = g_n^m(t = 2024.75) + 0.25\dot{g}_n^m(t = 2024.0), \quad (19)$$

where  $g_n^m$  are the SH coefficients of the internal field in nT and  $\dot{g}_n^m$  are the SH coefficients of the SV in nT yr<sup>-1</sup>. The SH coefficients for the internal field at epoch 2025.0 were output up to degree and order 13 with a numerical precision of 0.01 nT.

### 5.3 Predicted average secular variation 2025–2030

For the average SV between 2025 and 2030, we calculated the SV using the spline-based internal field of our parent model at epoch 2024.0, rather than at 2025.0, and we did not attempt an extrapolation. We chose 2024.0 to avoid effects due to the temporal regularization imposed on the internal field model and the lack of data for constraining the SV and the SA at the model endpoint.

## 6 Summary

We have presented the parent model for DTU's contributions to the IGRF-14. Our DGRF-2020 candidate is the internal field of the parent model directly evaluated at 2020.0, where good data coverage is available thanks to the *Swarm*, CryoSat2 and CSES satellites. Our candidate for the IGRF-2025 is the internal field of the parent model evaluated at 2024.75, at the end of the contributing satellite data, and linearly extrapolated to 2025.0 using the secular variation in 2024.0, when the last annual difference data from the ground observatories were available. The latter coefficients of secular variation also supply our candidate for the predictive SV in 2025–2030.

## 7 Acknowledgments

We wish to thank ESA for the prompt availability of Swarm L1b data and for providing access to the Cryosat2 platform magnetometer data and related engineering information. The support of the CHAMP mission by the German Aerospace Center (DLR) and the Federal Ministry of Education and Research is gratefully acknowledged. The Ørsted Project was made possible by extensive support from the Danish Government, NASA, ESA, CNES, DARA and the Thomas B. Thriges Foundation. The staff of the geomagnetic observatories and INTERMAGNET are thanked for supplying high-quality observatory data. We thank the China National Space Administration (CNSA) and the Italian Space Agency (ASI) for making the CSES magnetic data available. The China National Space Administration, the Macau Foundation and the Macau Institute of Space Technology and Application (MISTA), Macau University of Science and Technology are thanked for their support of the MSS-1 mission and for making the MSS-1 magnetic data available. BGS are gratefully acknowledged for collating checked and corrected observatory hourly mean values in the AUX\_OBS database. We wish to thank Karl-Magnus Laundal for helping with the implementation of the AMPS ionospheric field parameterization.

## References

- Alken, P. et al. (2021). “International Geomagnetic Reference Field: the thirteenth generation”. In: *Earth, Planets and Space* 73.1. DOI: [10.1186/s40623-020-01288-x](https://doi.org/10.1186/s40623-020-01288-x).

- Aubert, J. and C. C. Finlay (2019). “Geomagnetic jerks and rapid hydromagnetic waves focusing at Earth’s core surface”. In: *Nature Geoscience* 12.5, pp. 393–398.
- Aubert, J. and N. Gillet (2021). “The interplay of fast waves and slow convection in geodynamo simulations nearing Earth’s core conditions”. In: *Geophys. J. Int.* 225, pp. 1854–1873. DOI: [10.1093/gji/ggab054](https://doi.org/10.1093/gji/ggab054).
- Aubert, J., P. W. Livermore, C. C. Finlay, A. Fournier, and N. Gillet (2022). “A taxonomy of simulated geomagnetic jerks”. In: *Geophysical Journal International* 231, pp. 650–671. DOI: [10.1093/gji/ggac212](https://doi.org/10.1093/gji/ggac212).
- Aubert, Julien (2023). “State and evolution of the geodynamo from numerical models reaching the physical conditions of Earth’s core”. In: *Geophysical Journal International* 235.1, pp. 468–487. ISSN: 1365-246X. DOI: [10.1093/gji/ggad229](https://doi.org/10.1093/gji/ggad229).
- Finlay, C. C. et al. (2020). “The CHAOS-7 geomagnetic field model and observed changes in the South Atlantic Anomaly”. In: *Earth, Planets and Space*. DOI: [10.1186/s40623-020-01252-9](https://doi.org/10.1186/s40623-020-01252-9).
- Finlay, Christopher C., Nils Olsen, Stavros Kotsiaros, Nicolas Gillet, and Lars Tøffner-Clausen (2016). “Recent geomagnetic secular variation from Swarm and ground observatories as estimated in the CHAOS-6 geomagnetic field model”. In: *Earth, Planets and Space* 68.1. DOI: [10.1186/s40623-016-0486-1](https://doi.org/10.1186/s40623-016-0486-1).
- Finlay, Christopher C., Nils Olsen, and Lars Tøffner-Clausen (2015). “DTU candidate field models for IGRF-12 and the CHAOS-5 geomagnetic field model”. In: *Earth, Planets and Space* 67.1. DOI: [10.1186/s40623-015-0274-3](https://doi.org/10.1186/s40623-015-0274-3).
- Gillet, N, F Dall’Asta, and P Amblard R Claveau J Aubert (2024). “Waves in Earth’s core and geomagnetic field forecast”. In: *Physics of the Earth and Planetary Interiors*, (under review).
- Grayver, Alexander V et al. (2017). “Joint inversion of satellite-detected tidal and magnetospheric signals constrains electrical conductivity and water content of the upper mantle and transition zone”. In: *Geophysical Research Letters* 44.12, pp. 6074–6081.
- Holme, Richard and Jeremy Bloxham (1996). “The treatment of attitude errors in satellite geomagnetic data”. In: *Physics of the Earth and Planetary Interiors* 98.3-4, pp. 221–233.
- Huber, P. J. (2004). *Robust statistics*. Wiley Series in Probability and Statistics - Applied Probability and Statistics Section Series. Wiley. ISBN: 9780471650720.
- Laundal, K. M., C. C. Finlay, N. Olsen, and J. P. Reistad (2018). “Solar wind and seasonal influence on ionospheric currents from swarm and CHAMP measurements”. In: *Journal of Geophysical Research: Space Physics* 123.5, pp. 4402–4429. DOI: [10.1029/2018ja025387](https://doi.org/10.1029/2018ja025387).
- Laundal, Karl M., Christopher C. Finlay, and Nils Olsen (2016). “Sunlight effects on the 3D polar current system determined from low Earth orbit measurements”. In: *Earth, Planets and Space* 68.1, p. 142.
- Laundal, Karl Magnus and Arthur D. Richmond (2017). “Magnetic coordinate systems”. In: *Space Science Reviews* 206.1-4, pp. 27–59.
- Lütkepohl, H. (2005). *New introduction to multiple time series analysis*. Springer.
- Macmillan, S. and N. Olsen (2013). “Observatory data and the Swarm mission”. In: *Earth, Planets and Space* 65.11, pp. 1355–1362. DOI: [10.5047/eps.2013.07.011](https://doi.org/10.5047/eps.2013.07.011).
- Matzka, J., C. Stolle, Y. Yamazaki, O. Bronkalla, and A. Morschhauser (2021a). “The geomagnetic K<sub>p</sub> index and derived indices of geomagnetic activity”. In: *Space Weather*. DOI: [10.1029/2020sw002641](https://doi.org/10.1029/2020sw002641).
- Matzka, Jürgen, Oliver Bronkalla, Katrin Tornow, Kirsten Elger, and Claudia Stolle (2021b). *Geomagnetic K<sub>p</sub> index. V.1.0*. GFZ Data Services. DOI: [10.5880/Kp.0001](https://doi.org/10.5880/Kp.0001).
- Matzka, Jürgen et al. (2024). *Geomagnetic H<sub>p0</sub> index (V3.0)*. DOI: [10.5880/HPO.0003](https://doi.org/10.5880/HPO.0003).
- Newell, P. T., T. Sotirelis, K. Liou, C. I. Meng, and F. J. Rich (2007). “A nearly universal solar wind-magnetosphere coupling function inferred from 10 magnetospheric state variables”. In: *Journal of Geophysical Research: Space Physics* 112.A1. ISSN: 2156-2202. DOI: [10.1029/2006JA012015](https://doi.org/10.1029/2006JA012015).
- Olsen, Nils, Giuseppe Albini, Jerome Bouffard, Tommaso Parrinello, and Lars Tøffner-Clausen (2020). “Magnetic observations from CryoSat-2: calibration and processing of satellite platform magnetometer data”. In: *Earth, Planets and Space* 72, pp. 1–18.
- Olsen, Nils, Mioara Mandea, Terence J. Sabaka, and Lars Tøffner-Clausen (2009). “CHAOS-2 — a geomagnetic field model derived from one decade of continuous satellite data”. In: *Geophysical Journal International* 179.3, pp. 1477–1487. DOI: [10.1111/j.1365-246x.2009.04386.x](https://doi.org/10.1111/j.1365-246x.2009.04386.x).
- Olsen, Nils, Mioara Mandea, Terence J. Sabaka, and Lars Tøffner-Clausen (2010). “The CHAOS-3 geomagnetic field model and candidates for the 11th generation IGRF”. In: *Earth, Planets and Space* 62.10, pp. 719–727. DOI: [10.5047/eps.2010.07.003](https://doi.org/10.5047/eps.2010.07.003).
- Olsen, Nils et al. (2006). “CHAOS—a model of the Earth’s magnetic field derived from CHAMP, Ørsted, and SAC-C magnetic satellite data”. In: *Geophysical Journal International* 166.1, pp. 67–75.
- Olsen, Nils et al. (2014). “The CHAOS-4 geomagnetic field model”. In: *Geophysical Journal International* 197.2, pp. 815–827.
- Sabaka, Terence J., Lars Tøffner-Clausen, Nils Olsen, and Christopher C. Finlay (2018). “A comprehensive model of Earth’s magnetic field determined from 4 years of Swarm satellite observations”. In: *Earth, Planets and Space* 70.1. DOI: [10.1186/s40623-018-0896-3](https://doi.org/10.1186/s40623-018-0896-3).

- Schwintzer, P., L. Grunwaldt, and C. Förste (2002). *CHAMP reference systems, transformations and standards*. Tech. rep. GFZ German Research Centre for Geosciences.
- Sugiura, M. and T. Kamei (1991). “Equatorial Dst index 1957-1986”. In: *IAGA Bulletin No. 40*.
- Tøffner-Clausen, Lars and Jonas Nielsen (2019). *Swarm - Level 1b processor algorithms*. Tech. rep. SW-RS-DSC-SY-0002, Issue 6.11. Technical University of Denmark.
- Yamazaki, Y. et al. (2022). “Geomagnetic activity index Hpo”. In: *Geophysical Research Letters* 49.10. ISSN: 1944-8007. DOI: [10.1029/2022gl098860](https://doi.org/10.1029/2022gl098860).